Chemical Science

EDGE ARTICLE

View Article Online
View Journal | View Issue



Cite this: *Chem. Sci.*, 2014, **5**, 2702

# Novel hole transporting materials based on triptycene core for high efficiency mesoscopic perovskite solar cells†

Anurag Krishna,‡[abd] Dharani Sabba,‡[ad] Hairong Li,‡[a] Jun Yin,[c] Pablo P. Boix,[a] Cesare Soci,[c] Subodh G. Mhaisalkar*[ad] and Andrew C. Grimsdale*[d]

Received 19th March 2014
Accepted 25th April 2014

DOI: 10.1039/c4sc00814f

www.rsc.org/chemicalscience

Three novel hole-conducting molecules (**T101**, **T102** and **T103**) based on a triptycene core have been synthesized using short routes with high yields. The optical and electrochemical properties were tuned by modifying the functional groups, through linking the triptycene to diphenylamines *via* phenyl and/or thienyl groups. The mesoporous perovskite solar cells fabricated using **T102** and **T103** as the hole transporting material (HTM) showed a power conversion efficiency (PCE) of 12.24% and 12.38%, respectively, which is comparable to that obtained using the best performing HTM spiro-OMeTAD. The **T102** based device showed higher fill factor (69.1%) and $V_{oc}$ (1.03 V) than the spiro-OMeTAD based device (FF = 63.4%, $V_{oc}$ = 0.976 V) whereas the **T103** based device showed comparable $J_{sc}$ (20.3 mA cm$^{-2}$) and higher $V_{oc}$ (0.985 V) than the spiro-OMeTAD ($J_{sc}$ = 20.8 mA cm$^{-2}$) based cell.

## Introduction

In 1991, Grätzel and O'Regan developed the mesoscopic dye sensitized solar cell (DSSC), using a Ruthenium complex dye and nanocrystalline titania ($TiO_2$) mesoporous film with PCE ~7% efficiency.[1] This discovery opened a new frontier in the development of solar energy harvesting technologies. A typical DSSC consists of a nanocrystalline mesoporous $TiO_2$ film, a dye sensitizer, a redox electrolyte and counter electrode. Impressive efficiencies over 12% have been achieved in DSSC with liquid electrolyte.[2] However, the leakage problem, instability and corrosive nature of the redox electrolyte have emerged as the major impediments in the commercialization of DSSCs.[3] To get rid of these problems, the focus has been shifted to solid state devices in which the liquid electrolyte is replaced by a solid hole transporting material (HTM). In 1995 Tennakone *et al.*[4] reported p-type CuI as first HTM for solid state DSSCs (ssDSSCs), with device efficiency of 0.8%. In 2012, Sakamoto *et al.*[5] achieved PCE of 7.4% with CuI as HTM. In 2012 the Kanatzidis group achieved PCE ~8.5% using p-type semiconductor $CsSnI_3$ as HTM in ssDSSC.[6] The progress of inorganic HTMs for ss-DSSCs has, however, been slow mainly due to the limited choices of materials.

Consequently, the research focus gradually shifted to organic materials and in 1998, Bach *et al.* reported the first ssDSSC using an organic HTM-spiro-OMeTAD-with a PCE of 0.74%.[7] This was a major breakthrough in the development of ssDSSCs and since then spiro-OMeTAD has been extensively studied in ss-DSSCs.[8–15] Through a variety of manipulation and tuning of device components such as changing dyes, modifying the $TiO_2$ and developing new dopants for spiro-OMeTAD, in 2011 a record efficiency of 7.2% for a ssDSSC using spiro-OMeTAD was achieved by the Grätzel group.[15] Other HTMs apart from spiro-OMeTAD has been also investigated but have generally been less successful. In 2006, Durrant *et al.*[16] synthesized six HTMs based on triarylamine oligomers but all of them showed lower PCE as compared to spiro-OMeTAD. In 2006 Snaith *et al.*[17] synthesized a liquid hole transporting material tris-[4-(2-methoxy-ethoxy)-phenyl]-amine with a glass transition temperature of −14 °C, which showed PCE of only 2.4%. In 2012 O'Regan *et al.*[18] synthesized a low melting point HTM based on a hydrazone containing methoxy-substituted triphenylamine that can easily infiltrate mesoporous $TiO_2$ films, but a PCE of only 0.075% was obtained. Sellinger *et al.*[19] synthesized two HTMs based on fluorene and carbazole cores with low glass transition temperatures which showed PCEs comparable to the PCE obtained using spiro-OMeTAD. In 2011 Liu *et al.*[20] investigated several conjugated polymers in ssDSSCs, including polypyrrole, polyaniline, poly-(3-alkylthiophene), triarylamine-based polymer, poly[2-methoxy-5-(2-ethylhexyloxy)-1,4-phenylenevinylene] (MEHPPV), and poly(3,4-ethylenedioxythiophene) (PEDOT).

[a]*Energy Research Institute @ NTU (ERI@N), Research Techno Plaza, X-Frontier Block, Level 5, 50 Nanyang Drive, Singapore 637553. E-mail: Subodh@ntu.edu.sg*

[b]*Energy Research Institute, Interdisciplinary Graduate School, Nanyang Technological University, Singapore*

[c]*Division of Physics and Applied Physics, Nanyang Technological University, 21Nanyang Link, Singapore 637371*

[d]*School of Materials Science and Engineering, Nanyang Technological University, Nanyang Avenue, Singapore 639798. E-mail: acgrimsdale@ntu.edu.sg*

† Electronic supplementary information (ESI) available: $^1$H and $^{13}$C spectra for new compounds. See DOI: 10.1039/c4sc00814f

‡ These authors contributed equally to this work.

Poly(3-hexylthiophene) (P3HT) and PEDOT are the most studied among these polymers. A PCE of 6.8% was reported using PEDOT as the HTM.[21] Despite showing much initial promise ss-DSSCs failed to live up to expectations as a maximum PCE of only 7.2% has been achieved. To date spiro-OMeTAD remains the most widely used HTM in solid state devices, despite its high cost.

Recently, organic–inorganic lead halide perovskite compounds have replaced the dye as sensitizers in DSSC devices. The lead iodide perovskite derivatives have high extinction coefficients, direct bandgaps, large exciton diffusion lengths and excellent absorption throughout the UV-Vis-NIR spectrum.[22] In 2012 Grätzel, Park *et al.* reported lead iodide perovskite ($CH_3NH_3PbI_3$) sensitized mesoscopic solid solar cells with spiro-OMeTAD as HTM with a PCE of 9.7%.[23] Subsequent to this discovery, lead halide perovskite based solid state devices have been developing rapidly and a PCE >15% has been reported by the groups of Grätzel[24] and of Snaith[25] using spiro-OMeTAD as HTM. To date promising, but slightly inferior, results have been obtained from other small molecules HTMs based on ethylenedioxythiophene,[26] cruciform oligothiophenes[27] and pyrene.[28] Less successful has been the use of conjugated polymers such as P3HT, poly[*N*-9-heptadecanyl-2,7-carbazole-*alt*-3,6-bis(thiophen-5-yl)-2,5-dioctyl-2,5-dihydropyrrolo-[3,4]pyrrole-1,4-dione] (PCBTDPP), poly-[2,1,3-benzothiadiazole-4,7-diyl[4,4-bis(2-ethylhexyl)-4*H*-cyclopenta[2,1-*b*:3,4-*b*′]dithiophene-2,6-diyl]] (PCPDTBT), poly[[9-(1-octylnonyl)-9*H*-carbazole-2,7-diyl]-2,5-thiophene-diyl-2,1,3-benzothiadiazole-4,7-diyl-2,5-thiophenediyl] (PCDTBT), and poly(triarylamine) (PTAA) as HTMs.[29] However, the high cost of spiro-OMeTAD and the lower performance of other HTMs impedes the growth and advancement of high efficiency cost-effective perovskite solar cells. Hence it is imperative to find alternative HTMs to spiro-OMeTAD, which have better or comparable efficiency and are more economic.

Here we report three novel HTMs based on a triptycene central core (Fig. 1). All three were synthesized from a relatively inexpensive commercially available triptycene derivative in a few steps with high overall yields. The bulky and twisted structure of triptycene has some similarity to that of spiro-OMeTAD and provides high thermal stability, high glass transition temperature ($T_g$) and high solubility in common organic solvents.[30] In this work we investigated the performance of these three materials in perovskite solar cells as the HTMs in comparison to similar devices using spiro-OMeTAD as HTM.

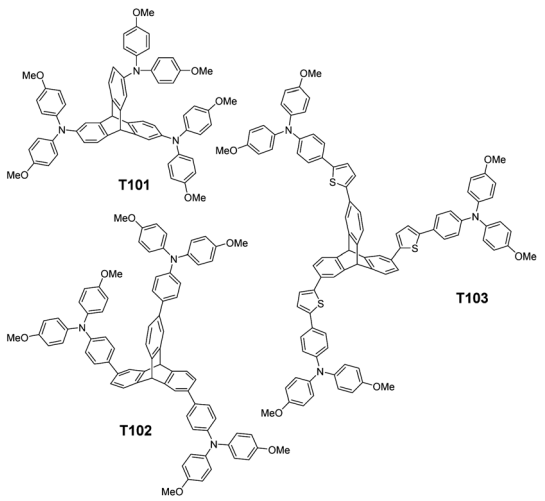


Fig. 1 Chemical structures of T101, T102 and T103.

## Results and discussion

### Synthesis

Compounds **1**[30,31] and **5**[32] were synthesized according to the literature procedures.

**2,6,14-Tri(*N*,*N*-bis(4-methoxyphenyl)amino)-triptycene (T101).** Compound **1** (1 g, 1.58 mmol), compound **2** (1.08 g, 4.74 mmol), *t*-BuOK (1.06 g, 9.48 mmol), P(*t*-Bu)$_3$HBF$_4$ (90 mg, 0.31 mmol) and Pd(dba)$_2$ (0.18 g, 0.31 mmol) were put into a 50 mL round bottom flask (RBF) and degassed using $N_2$. Dry toluene (20 mL) was degassed using $N_2$ and then injected into the RBF. The reaction mixture was then stirred at 80 °C for 2 days. The reaction mixture was cooled to RT and toluene was removed using a rotary evaporator. The reaction mixture was then extracted with dichloromethane (DCM) and washed with water. The DCM layer was dried over anhydrous $MgSO_4$, concentrated and the residue mixture was purified by column chromatography on silica gel eluting with DCM/hexane = 2/1 (v/v) to obtain the product as a white fluffy solid (0.85 g, 75%). $^1$H NMR ($CD_2Cl_2$) $\delta$: 6.92–7.10 (br, m, 18H, MeOPh*H* and triptycene*H*), 6.81–6.84 (m, 12H, MeOPh*H*), 6.54 (br, 3H, triptycene*H*), 5.05 (s, 1H, bridge-C*H*), 4.95 (s, 1H, bridge-C*H*), 3.79 (s, 18H, OC$H_3$). $^{13}$C NMR ($CD_2Cl_2$) $\delta$: 156.2, 147.4, 146.9, 141.6, 126.9, 124.2, 123.9, 117.3, 117.0, 116.7, 115.0, 55.8, 52.9. MALDI-TOF calcd for $C_{62}H_{53}N_3O_6$, 935.39; found, 935.35. Anal. calcd for $C_{62}H_{53}N_3O_6$: C, 79.55; H, 5.71; N, 4.49. Found: C, 79.36; H, 5.76; N, 4.57%.

**2,6,14-Tri(*N*,*N*-bis(4-methoxyphenyl)amino-phen-4-yl)-triptycene (T102).** Compound **1** (0.2 g, 0.32 mmol), compound **5** (0.39 g, 1.11 mmol), Pd(0)(PPh$_3$)$_4$ (0.12 g, 0.1 mmol), degassed toluene (20 mL) and 2 M $K_2CO_3$ (5 mL) were transferred in to a 50 mL RBF. The reaction mixture was then stirred at 80 °C under nitrogen for 1 day. The reaction mixture was cooled down to r.t. and poured into water, extracted with DCM and washed with water. The DCM layer was dried over $MgSO_4$, concentrated and the residue mixture was purified by column chromatography on silica gel eluting with DCM/hexane = 2/1 (v/v) to obtain the product as a white solid (0.34 g, 90%). $^1$H NMR ($CDCl_3$) $\delta$: 7.61 (br, 3H, triptycene*H*), 7.44 (d, $J$ = 7.6 Hz, 3H, triptycene*H*), 7.28–7.35 (m, 5H, triptycene*H*, Ph*H*), 7.18–7.21 (m, 6H, Ph*H*), 7.08 (br, 10H, Ph*H*), 6.96 (br, 6H, Ph*H*), 6.85 (d, $J$ = 8.4 Hz, 12H, Ph*H*), 5.54 (s, 2H, bridge-C*H*), 3.81 (s, 18H, OC$H_3$). $^{13}$C NMR ($CDCl_3$) $\delta$: 156.6, 146.4, 144.2, 141.6, 138.9, 138.5, 129.7, 128.9, 128.2, 127.2, 126.0, 124.5, 124.1, 122.8, 121.4, 115.3, 56.1, 54.8, 54.2. MALDI-TOF calcd for $C_{80}H_{65}N_3O_6$, 1163.49; found, 1163.48. Anal. calcd for $C_{80}H_{65}N_3O_6$: C, 82.52; H, 5.63; N, 3.61. Found: C, 82.38; H, 5.66; N, 3.64%.

**2,6,14-Tri(thien-2-yl)-triptycene (4).** Compound **1** (1 g, 1.58 mmol), compound **3** (2.36 g, 6.33 mmol), Pd(PPh$_3$)$_2$Cl$_2$ (90 mg, 0.13 mmol) and degassed 25 mL tetrahydrofuran (THF) were

added into a 50 mL RBF and the reaction was stirred at 70 °C under $N_2$ for 12 h. The reaction solution was cooled down and the THF was removed under reduced pressure. The crude was purified by column chromatography on silica gel eluting with DCM/hexane = 1/3 (v/v) to obtain the product as a white solid (0.7 g, 90%). $^1$H NMR ($CDCl_3$) $\delta$: 7.68 (s, 3H, triptycene*H*), 7.66 (s, 3H, triptycene*H*), 7.41–7.44 (m, 3H, triptycene*H*), 7.22–7.29 (m, 6H, Th*H*), 7.02–7.04 (m, 3H, Th*H*), 5.51 (s, 1H, bridge-C*H*), 5.49 (s, 1H, bridge-C*H*). $^{13}$C NMR ($CDCl_3$) $\delta$: 146.1, 145.0, 144.6, 132.5, 128.5, 125.2, 124.8, 124.7, 123.9, 123.8, 123.6, 122.4, 122.3, 54.4, 54.0. MALDI-TOF calcd for $C_{32}H_{20}S_3$, 500.07; found, 500.04.

**2,6,14-Tri(5′-(*N*,*N*-bis(4-methoxyphenyl)aminophen-4-yl)thiophene-2-yl)-triptycene (T103).** Compound **4** (0.2 g, 0.4 mmol) and *N*-bromosuccinimide (NBS) (0.22 g, 1.23 mmol) were dissolved in 20 mL freshly distilled THF and stirred at r.t. for 6 h under $N_2$. Then the solution was poured into water, stirred for few minutes and filtered. The collected white solid **6** was dried and transferred into a 50 mL RBF together with compound **5** (0.55 g, 1.2 mmol) to carry out Suzuki coupling following the same procedure to make **T102**. The **T103** was obtained as a yellow solid with yield of 80%. $^1$H NMR ($CD_2Cl_2$) $\delta$: 7.72 (d, $J$ = 5.2 Hz, 3H, triptycene*H*), 7.34–7.48 (m, 9H, Ph*H*, triptycene*H*), 7.32 (d, $J$ = 7.6 Hz, 3H, triptycene*H*), 7.25 (d, $J$ = 3.6 Hz, 3H, Th*H*), 7.16 (d, $J$ = 3.6 Hz, 3H, Th*H*), 7.09 (d, $J$ = 8.8 Hz, 12H, Ph*H*), 6.86–6.92 (m, 18H, Ph*H*), 5.56 (s, 1H, bridge-C*H*), 5.54 (s, 1H, bridge-C*H*), 3.81 (s, 18H, OC$H_3$). $^{13}$C NMR ($CD_2Cl_2$) $\delta$: 156.7, 148.8, 146.0, 144.3, 144.0, 142.4, 140.9, 132.3, 131.3, 127.2, 126.59, 126.55, 124.49, 124.40, 122.9, 121.4, 121.3, 120.6, 115.1, 68.2, 65.9, 55.9. MALDI-TOF calcd for $C_{92}H_{71}N_3O_6S_3$, 1410.45; found, 1410.46. Anal. calcd for $C_{92}H_{71}N_3O_6S_3$: C, 78.33; H, 5.07; N, 2.98; S, 6.82. Found: C, 78.25; H, 5.05; N, 3.09, S, 6.77% (Scheme 1).

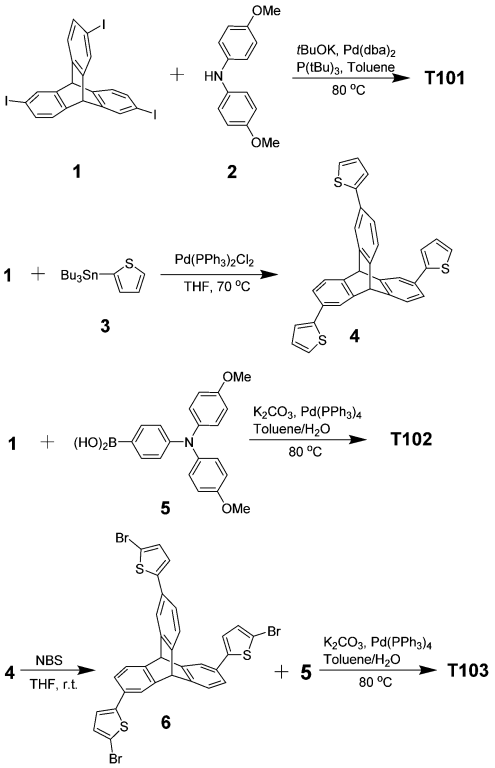


Scheme 1 Synthetic route to T101–T103.

## Modelling and quantum chemistry calculations

Quantum chemistry calculations were used to predict the electronic and optical properties of our triptycene-based materials. As shown in Fig. 2 and Table 1, LUMOs of **T101**, **T102** and **T103** decrease with little shift in the HOMO levels upon extension of the molecular conjugated length using linking groups between the central triptycene and terminal diphenylamine groups (benzene for **T102**, benzene and thiophene for **T103**). It was also found that the calculated variety of trends of HOMO, LUMO levels and ionization potentials coincides well with the experimental data. As in the case of spiro-OMeTAD,[33] the HOMOs of the triptycene-based materials delocalize over the whole molecule, while the LUMOs are largely localized on the diphenylamine units in **T101** or on the linking groups in **T102** and **T103**. This is different from the case of spiro-OMeTAD, where the LUMO localizes on the central spiro-group. In triptycene-based materials, the partial wave function overlap between LUMO and HOMO leads to a strong Coulomb interaction, which can favor formation of neutral excitons and hole transport. The calculated hole reorganization energies ($\lambda_{hole}$) of these triptycene-based materials (80–120 meV) are much smaller than typical hole-transporting spiro-OMeTAD (148 meV), showing potential of

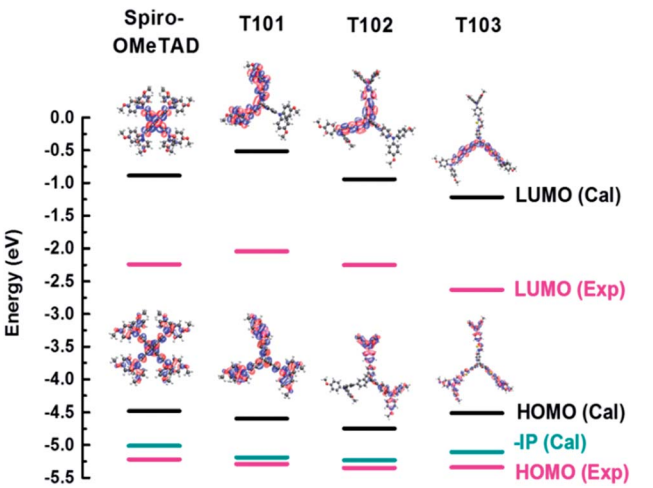


Fig. 2 Calculated and experimental ionization potential (IP), HOMO, LUMO levels and electronic density distributions of spiro-OMeTAD and triptycene-based HTMs **T101**, **T102** and **T103**.

**T101**, **T102** and **T103** as hole-transporting materials in perovskite-based solar cells.

The calculated and experimental absorption spectra of our triptycene-based materials are shown in Fig. 3. The CAM-B3LYP method is well-known to overestimate the excitation energy but usually gives results closer to the experimental data than do hybrid GGA functionals such as B3LYP. Our TD-DFT calculations can help interpret the fundamental absorption peak as an electronic transition, where the individual excited states can be

 

Table 1 Summary of the calculated and experimental optical and electronic properties

| | Calculated data | | | | | | Experimental data | | | |
|---|---|---|---|---|---|---|---|---|---|---|
| Molecule | LUMO (eV) | HOMO (eV) | −IP[a] (eV) | $E_g$[b] (eV) | $\lambda_{hole}$ (meV) | $\lambda_{electron}$ (meV) | $\lambda_{max}$ (nm) | $E_{opt.gap}$[c] (eV) | LUMO[d] (eV) | HOMO (eV) |
| Spiro-OMeTAD | −0.61 | −4.21 | −5.01 | 3.72 | 148 | 334 | 385 | 2.98 | −2.24 | −5.22 |
| **T101** | −0.52 | −4.60 | −5.19 | 4.17 | 119 | 112 | 302 | 3.25 | −2.04 | −5.29 |
| **T102** | −0.94 | −4.75 | −5.23 | 3.99 | 83 | 328 | 340 | 3.10 | −2.25 | −5.35 |
| **T103** | −1.22 | −4.51 | −5.11 | 3.43 | 87 | 333 | 388 | 2.71 | −2.62 | −5.33 |

[a] Ionization potential (IP) calculated by total energy difference of $E_{cation} - E_{neutral}$. [b] $S^0 \rightarrow S^1$ excitation energy determined by the TDDFT/CAM-B3LYP method. [c] Optical gap determined from UV absorption onset. [d] $E_{LUMO} = E_{HOMO} + E_{opt.gap}$.

further analysed using natural transition orbitals (NTOs),[34,35] giving a simple orbital picture of the results of TD-DFT calculations by representing each electronic transition in terms of two orbitals (electron and hole). The transition carries the largest oscillator strength leading to the high-energy absorption band in these hole transporting materials, which constitutes the lowest-energy absorption band in the experimental spectrum. The corresponding dominant NTOs in Fig. S9 in ESI† clearly show its significant charge-transfer (CT) character with the central triptycene unit acting as an electron acceptor for given optical transitions from the ground to excited states.

### Thermal, optical and electrochemical properties

The UV-Vis absorption spectra of **T101**, **T102** and **T103** are shown in Fig. 3. **T101**, **T102** and **T103** exhibit absorption peak centered at 305, 340 and 390 nm, respectively. The spectra of **T102** and **T103** red shifted as compared to **T101**, which can be attributed to increase in π-conjugation. In **T102** π-conjugation is extended by inserting phenyl ring in between triptycene and diphenylamine moieties whereas in **T103** by inserting thienyl groups. The optical band gap ($E_g$) is calculated from the absorption onset wavelength of the corresponding absorption spectrum. The onset wavelengths for **T101**, **T102**, **T103** and spiro-OMeTAD are 381, 400, 458 and 420 nm, which corresponds to optical band gap ($E_g$) of 3.25, 3.1, 2.71 and 2.98 eV for **T101**, **T102**, **T103**, and spiro-OMeTAD respectively.

Cyclic voltammograms of **T101**, **T102**, and **T103** are shown in Fig. 4. The pair of redox peaks of all the HTMs is highly reversible, showing that it has excellent electrochemical stability. Further, HOMO energy level is calculated from the CV data using the following equation: $E_{HOMO} = -5.1 - (E_{ox,HTM}$ *vs.* $Fc/Fc^+)$ (eV), where $E_{ox,HTM}$ *vs.* $Fc/Fc^+$ is the onset of oxidation potential with reference to ferrocene.[36] The HOMO levels of **T101**, **T102** and **T103** calculated from CV are −5.29, −5.35 and −5.33 eV, respectively. The reported HOMO energy level for $CH_3NH_3PbI_3$ is −5.44 eV,[23] which indicates that all the HTMs have energetics favorable for hole transfer. Table 1 summarizes the optical and electrochemical properties of the three HTMs. Spiro-OMeTAD has HOMO of −5.22 eV which smaller as compared to all our triptycenes. As the difference between the Fermi level of $TiO_2$ and HOMO of HTM determines open circuit voltage ($V_{oc}$) of the cell, higher $V_{oc}$ is expected for all the new HTMs especially **T102**. The measured Differential Scanning Calorimetry (DSC) results were plotted in Fig. 5. DSC data shows $T_g$ of 120, 140 and 108 °C for **T101**, **T102** and **T103**, respectively; while the $T_g$ of spiro-OMeTAD was reported to be 120 °C.[7] The $T_g$ values among the three triptycenes varied significantly, which

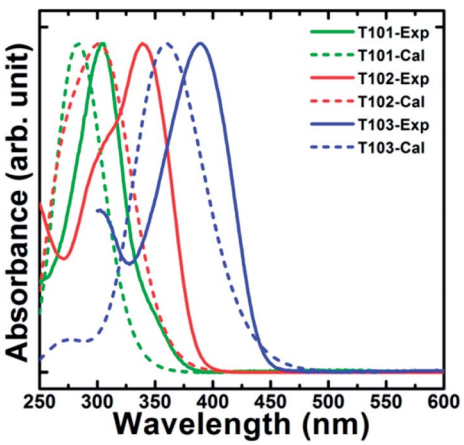


Fig. 3 Calculated and experimental absorption spectra of triptycene-based materials (T101, T102 and T103).

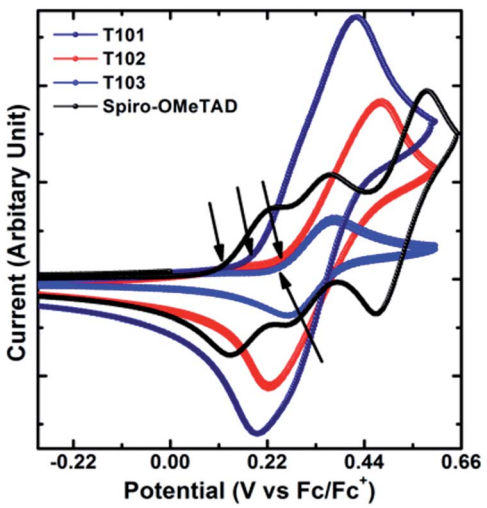


Fig. 4 Cyclic voltagrams of spiro-OMeTAD, T101, T102 and T103 with ferrocene as the reference.

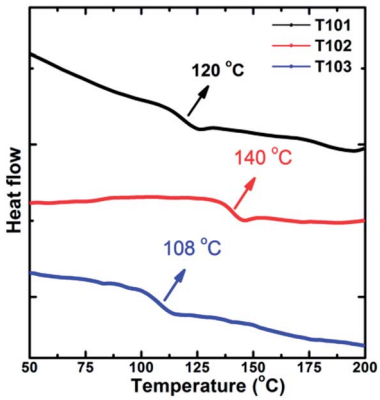


Fig. 5 Differential Scanning Calorimetry (DSC) curves of **T101**, **T102** and **T103**.

can be attributed to the subtle interplay between the twisted bulky side groups and the rigid triptycene core. The high $T_g$ values indicate that all the HTMs are amorphous and have good thermal stability.

## Device performance

Cross-section SEM picture shown in Fig. 6(a) illustrates the typical solid state solar cell device based on perovskite as inorganic sensitizer. The current–density–voltage ($J$–$V$) characteristics of the devices employing **T101**, **T102**, **T103** and spiro-OMeTAD, together with a device without HTM are shown in Fig. 6(b). The device performance data is summarized in Table 2.

The PCE of the device with **T101**, **T102**, **T103** and spiro-OMeTAD as HTM is 8.42%, 12.24%, 12.38% and 12.87%, respectively. The device fabricated without HTM shows PCE of only 4.69%, which confirms that an HTM must be an integral component of the device for obtaining high PCE. The short circuit current ($J_{sc}$) of the cells fabricated from **T101**, **T102**, **T103** and spiro-OMeTAD are 13.5, 17.2, 20.3 and 20.8 mA cm$^{-2}$, respectively. The $J_{sc}$ are well matched with the integrated $J_{sc}$ obtained from IPCE spectra as shown in Fig. 7 and also show similar trends. The similar shapes of the IPCEs for all the samples suggest that HTM absorption has negligible effect on the device performance. Impedance spectroscopy was performed to the spiro-OMeTAD, **T102** and **T103** based devices in order to elucidate the differences in the working mechanisms arising in similar performances. The fitting of the results followed previous models employed in perovskites solar cells, where the high frequency part of the impedance spectrum is attributed to the hole transport in the HTM, whereas the resistance of the lower frequency feature is determined by the recombination process.[37–39] The maximum splitting of the Fermi levels for photogenerated electrons and holes defines the $V_{oc}$. As a result, it is determined by the energetics (in our case, the different positions of the HTMs HOMO), the amount of photogenerated charge and the recombination. For both **T102** and **T103** based devices, the obtained $V_{oc}$ are slightly higher than those of spiro-OMeTAD-based device. The first one, **T102**, presents similar recombination resistance as spiro-OMeTAD

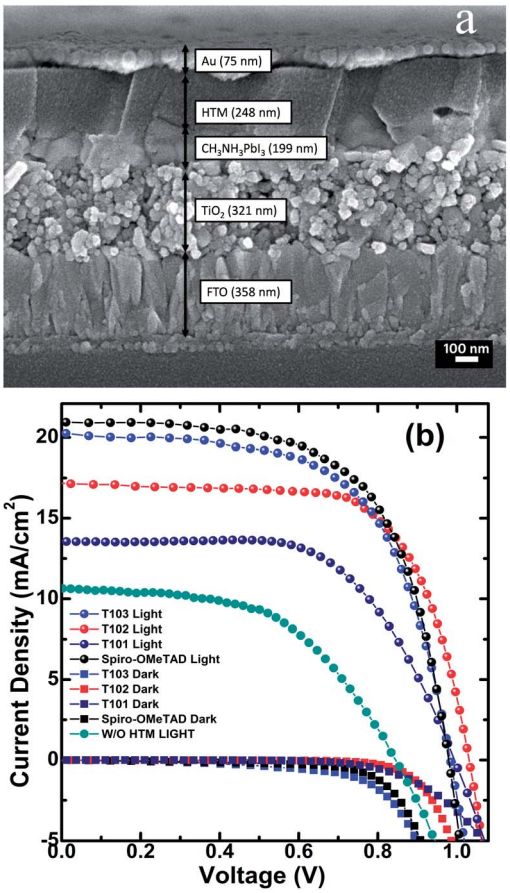


Fig. 6 (a) Cross-sectional SEM of the device; (b) Current density *vs.* voltage curve of lead iodide perovskite mesoscopic solar cells with HTMs **T101**, **T102**, **T103**, Spiro-OMeTAD and without any HTM.

Table 2 Summary of device parameters; current density ($J_{sc}$), open circuit voltage ($V_{oc}$), fill factor (FF) and efficiency ($\eta$)

| HTM | $J_{sc}$ (mA cm$^{-2}$) | $V_{oc}$ (V) | FF (%) | PCE, $\eta$ (%) |
|---|---|---|---|---|
| Spiro-OMeTAD | 20.8 | 0.976 | 63.4 | 12.87 |
| **T103** | 20.3 | 0.985 | 61.9 | 12.38 |
| **T102** | 17.2 | 1.03 | 69.1 | 12.24 |
| **T101** | 13.5 | 0.996 | 62.6 | 8.42 |
| Without HTM | 10.6 | 0.844 | 52.5 | 4.69 |

device (see Fig. 8a), which should not make a difference in the achieved potential. Additionally, it has lower charge generation, as can be inferred from the lower $J_{sc}$, and ~130 meV deeper HOMO. Both opposite factors result in a higher $V_{oc}$ for the solar cells with the novel material.

The case of **T103** is different: although the solar cells based on this material present similar charge generation (*i.e.* photocurrent) than the spiro-OMeTAD-based one, the ~110 meV extra potential expected from the HOMO level shift is not reflected in the cell performance. The cause for this can be found in the recombination of the devices. Fig. 8a shows the recombination resistance of the devices, where the higher recombination for **T103** device is clear.

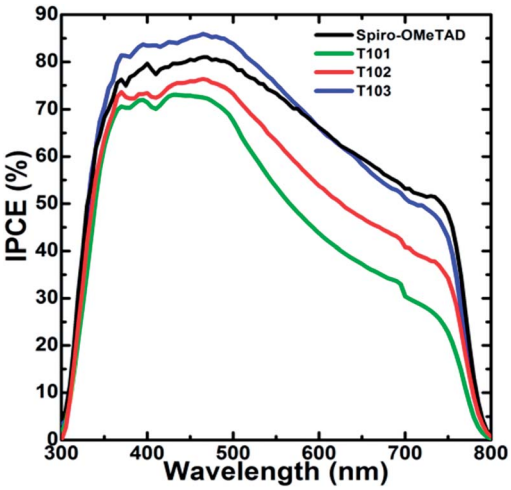


Fig. 7 IPCE spectra of the perovskite solar cell devices with **T101**, **T102** **T103** and spiro-OMeTAD as HTM, respectively.

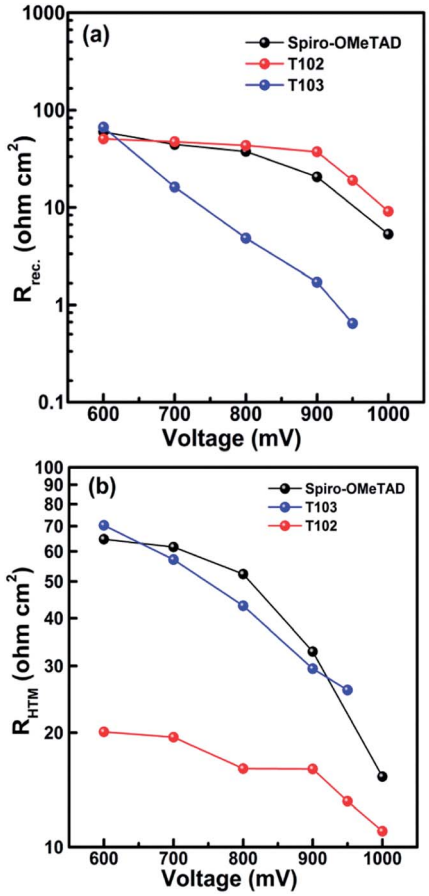


Fig. 8 (a) Recombination resistance and (b) transport resistance of HTMs in the full solar cell determined by electrochemical impedance spectroscopy.

Another remarkable difference in the performance is the higher fill factor higher for the **T102** device. The fill factor can be explained on the basis of series resistances (Fig. 8b) and recombination (Fig. 8a), which were studied by means of impedance spectroscopy. The devices with **T102** have lower HTM resistance than **T103** and spiro-OMeTAD ones, which explains the higher fill factor achieved by these samples. Whereas the HTM resistances of **T103** and spiro-OMeTAD are similar, the higher recombination of the **T103** device results in a slightly lower fill factor.

## Experimental

### Materials and equipments

Reactants and reagents, unless otherwise stated, were purchased either from Sigma-Aldrich or Alfa-Aesar, and used without further purification. Both absorption and reflection $TiO_2$ pastes were purchased from Dyesol. Column chromatography was carried out using Merck silica (230–400 mesh) while thin layer chromatography (TLC) was performed on Merck silica 60 Al-backed plates (20 cm × 20 cm). 1H and 13C NMR data were obtained on a Bruker DPX 400 MHz and 100 MHz spectrometer with chemical shifts referenced to $CDCl_3$ or $CD_2Cl_2$. Matrix assisted laser desorption/ionization time-of-flight (MALDI-TOF) mass spectra were obtained on a Shimadzu Biotech AXIMA-TOF. Elemental analysis was obtained *via* a Thermo Scientific Flash 2000 Series CHNS/O Analyzer. UV-Vis absorption spectra were recorded using Shimadzu UV-2501PC Spectrometer. Cyclic voltammetry (CV) experiments were performed on CHI411 electrochemical workstation. All CV measurements were recorded in dichloromethane (DCM) with 0.1 M tetrabutylammonium hexafluorophosphate as supporting electrolyte (scan rate of 100 mV $s^{-1}$). The experiments were performed at room temperature with a conventional three electrodes configuration consisting of a platinum wire working electrode, a gold counter electrode, and an Ag/AgCl in 3 M KCl reference electrode. Differential scanning calorimetry (DSC) was done using TA Instrument Q10. For the photovoltaic measurements, the solar cells having 0.2 $cm^{-2}$ active area were measured with 0.25 $cm^{-2}$ metal mask using solar simulator (San-EI Electric, XEC-301S) under AM 1.5G standard. *J–V* characteristics were recorded by applying external potential bias while measuring the current response with a Keithley 2612A SourceMeter. For electrochemical impedance spectroscopy study, measurements were carried out using AutoLab PGSTAT302N under illumination condition and different bias potentials were applied ranging from 0.05 V to open-circuit voltage and frequencies between 1 MHz and 0.1 Hz. Incident photon current efficiency studies was carried out using PVE300 from Bentham, with dual xenon/quartz halogen light source, measured in DC mode. The cross-sectional view of the devices was obtained with a field-emission scanning electron microscopy (FESEM, JOEL JSM 7600F).

### Device fabrication

Laser etched fluorine doped tin oxide (FTO, <14 ohm per square, 2.2 mm thick, Pilkington) glass substrates were cleaned with decon soap solution and ethanol respectively. Then a compact $TiO_2$ blocking layer was deposited on these substrates by aerosol spray-pyrolysis at 450 °C using ambient air as the

carrier gas. A solution of titanium diisopropoxide bis(acetylacetonate) (75 wt% in isopropanol) and absolute ethanol was used in the ratio 1 : 9 by volume. Then the substrates were calcined at 500 °C for 1 h. This blocking layer is about 80 nm thick. These substrates were further treated with 40 mM of $TiCl_4$ solution (Wako Reagent) for 30 min at 70 °C, followed by rinsing with deionized water and ethanol. The mesoporous $TiO_2$ layer composed of 30 nm-sized particles was deposited by spin coating at 4000 r.p.m. for 30 s using a commercial $TiO_2$ paste (Dyesol DSL 30 NRD) diluted in ethanol (1 : 3.5, weight ratio). After drying at 125 °C for 10 min, the $TiO_2$ films were gradually heated to 500 °C, baked at this temperature for 15 min and cooled to room temperature. Sequential method has been employed to deposit hybrid organic–inorganic perovskite $(CH_3NH_3)PbI_3$ on the $TiCl_4$ (40 mM, 70° C for 30 min) treated mesoporous $TiO_2$ films. Lead iodide (1 M) was dissolved in *N*,*N*-dimethylformamide under stirring conditions at 70 °C and the hot solution was spincoated on the substrates at 6000 r.p.m for 5 s. These substrates were then dried for 30 min at 70 °C. Subsequently the films were dipped in 8 mg $mL^{-1}$ solution of $CH_3NH_3I$ in 2-propanol for 20 min and rinsed with 2-propanol. Drying of the perovskite loaded substrates was done by spin-coating the substrates at 4000 rpm for 30 s followed by drying at 70 °C for 30 min. The organic hole conductors spiro-OMeTAD (100 mg $mL^{-1}$, International Laboratory USA), **T101**, **T102** and **T103** were dissolved in chlorobenzene (80–110 mg $mL^{-1}$) respectively and spincoated on these substrates. Additives like $Li(CF_3SO_2)_2N$, *tert*-butylpyridine and tris(2-(1*H*-pyrazol-1-yl) pyridine)cobalt(III) (FK 102) dopant were added to the above solution following a literature procedure.[24] A gold electrode of about 75 nm was deposited *via* thermal evaporator and an active area of 0.2 $cm^2$ was defined.

### Quantum chemistry calculations

Density functional theory calculations (DFT) were performed to optimize the geometries and study the electronic properties of ground state based on functional B3LYP with basis sets 6-31G(d,p), which provides correct description of the neutral states in extended π-conjugated systems. The absorption spectra and corresponding excitation energies were evaluated using the time-dependent density functional theory (TDDFT) based on range-separated DFT functional CAM-B3LYP/6-31G(d,p) method. Unrestricted DFT was performed for the cations and anions. The solvent effects were also taken into consideration here using the conductor-like polarizable continuum model (CPCM) with the dielectric constants of dichloromethane ($\varepsilon = 8.93$). The internal reorganization energy ($\lambda$) was calculated by $\lambda_{hole/electron} = E^{\pm}(N) - E^{\pm}(C) + E(C) - E(N)$,[40] where $E^{\pm}(N)$ is the energy of charged molecule (cation or anion) calculated using an optimal geometry of the neutral molecule, $E(C)$ is the energy of the neutral molecule in the geometry optimized for charged molecule, and $E(N)$ and $E^{\pm}(C)$ are the energies of the neutral and charged molecules at their corresponding optimal geometries. In this study, for these novel triptycene-based materials, the limited values of electronic coupling are expected due to the intermolecular charge-transfer processes involving direct contacts in amorphous solids. Therefore the hole (or electron) mobility can be dominated by the reorganization energy without regard for the electronic coupling. All calculations were carried out using the Gaussian09 program.

## Conclusion

We have designed and synthesized a series of novel HTMs based on a triptycene core, with very promising device performance which is comparable to the performance of cells fabricated with the most widely used spiro-OMeTAD while offering much simpler synthesis, potentially much lower production costs. Devices fabricated from **T102** and **T103** show PCE of 12.24 and 12.38%, which are comparable to that of a spiro-OMeTAD based device (PCE = 12.87%). So far all the conditions were based on those applied to spiro-OMeTAD. We are confident that detailed investigations in understanding the structure–property relationship and fine tuning of parameters such as film thickness, customized $TiO_2$ paste, solvent, heat treatment and dopant (kind and concentration) will boost the performance further.

## Acknowledgements

This work was funded by National Research Foundation (NRF), Singapore. (CRP Award no.: NRF-CRP4-2008-03).

## Notes and references

1 B. O'Regan and M. Grätzel, *Nature*, 1991, **353**, 737.
2 C. Y. Hsu, Y. C. Chen, R. Y. Yung Lin, K. C. Ho and J. T. Lin, *Phys. Chem. Chem. Phys.*, 2012, **14**, 14099.
3 A. Yella, H. W. Lee, H. N. Tsao, C. Yi, A. K. Chandiran, M. K. Nazeeruddin, E. W. G. Diau, C. Y. Yeh, S. M. Zakeeruddin and M. Grätzel, *Science*, 2011, **334**, 629.
4 K. Tennakone, G. R. R. A. Kumara, A. R. Kumarasinghe, K. G. U. Wijayantha and P. M. Sirimanne, *Semicond. Sci. Technol.*, 1995, **10**, 1689.
5 H. Sakamoto, S. Igarashi, M. Uchida, K. Niume and M. Nagai, *Org. Electron.*, 2012, **13**, 514.
6 I. Chung, B. Lee, J. He, R. P. H. Chang and M. G. Kanatzidis, *Nature*, 2012, **485**, 486.
7 U. Bach, D. Lupo, P. Comte, J. E. Moser, F. Weissortel, J. Salbeck, H. Spretizer and M. Grätzel, *Nature*, 1998, **395**, 583.
8 U. Bach, Y. Tachibana, J.-E. Moser, S. A. Haque, J. R. Durrant, M. Grätzel and D. R. Klug, *J. Am. Chem. Soc.*, 1999, **121**, 7445.
9 J. Krüger, U. Bach and M. Grätzel, *Adv. Mater.*, 2000, **12**, 447.
10 J. Krüger, R. Plass, M. Grätzel, P. J. Cameron and L. M. Peter, *J. Phys. Chem. B*, 2003, **107**, 7536.
11 J. Kirkpatrick and J. Nelson, *J. Chem. Phys.*, 2005, **123**, 084703.
12 H. J. Snaith and M. Grätzel, *Adv. Mater.*, 2007, **19**, 3643.
13 J. Melas-Kyriazi, I. K. Ding, A. Marchioro, A. Punzi, B. E. Hardin, G. F. Burkhard, N. Tétreault, M. Grätzel, J.-E. Moser and M. D. McGehee, *Adv. Energy Mater.*, 2011, **1**, 407.

 

14 X. Jiang, K. M. Karlsson, E. Gabrielsson, E. M. J. Johansson, M. Quintana, M. Karlsson, L. Sun, G. Boschloo and A. Hagfeldt, *Adv. Funct. Mater.*, 2011, **21**, 2944.
15 J. Burschka, A. Dualeh, F. Kessler, E. Baranoff, N. L. Cevey-Ha, C. Yi, M. K. Nazeerudin and M. Grätzel, *J. Am. Chem. Soc.*, 2011, **133**, 18042.
16 J. E. Kroeze, N. Hirate, L. Schmidt-Mende, C. Orizu, S. D. Ogier, K. Carr, M. Grätzel and J. R. Durrant, *Adv. Funct. Mater.*, 2006, **16**, 1832.
17 H. J. Snaith, S. M. Zakeeruddin, Q. Wang, P. Pechy and M. Grätzel, *Nano Lett.*, 2006, **6**, 2000.
18 M. Juozapavicius, B. C. O'Regan, A. Y. Anderson, J. V. Grazulevicius and V. Mimaite, *Org. Electron.*, 2012, **13**, 23.
19 T. Leijtens, I. K. Ding, T. Giovenzana, J. T. Bloking, M. D. McGehee and A. Sellinger, *ACS Nano*, 2012, **6**, 1455.
20 W. Zhang, Y. Cheng, X. Yin and B. Liu, *Macromol. Chem. Phys.*, 2011, **212**, 15.
21 J. Kim, J. K. Koh, B. Kim, S. H. Ahn, H. Ahn, D. Y. Ryu, J. H. Kim and E. Kim, *Adv. Funct. Mater.*, 2011, **21**, 4633.
22 A. Kojima, K. Teshima, Y. Shirai and T. Miyasaka, *J. Am. Chem. Soc.*, 2009, **131**, 6050.
23 H. Kim, J. H. Im, C. R. Lee, K. B. Lee, T. Moehl, A. Marchioro, S. J. Moon, R. H. Baker, J. H. Yum, J. E. Moser, M. Grätzel and N. G. Park, *Sci. Rep.*, 2012, **338**, 643.
24 J. Burschka, N. Pellet, S. J. Moon, R. H. Baker, P. Gao, M. K. Nazeeruddin and M. Grätzel, *Nature*, 2013, **499**, 316.
25 M. Liu, M. B. Johnston and H. J. Snaith, *Nature*, 2013, **501**, 395.
26 H. Li, K. Fu, A. Hagfeldt, M. Grätzel, S. G. Mhaisalkar and A. C. Grimsdale, *Angew. Chem., Int. Ed.*, 2014, **53**, 4085.
27 T. Krishnamoorthy, K. Fu, P. P. Boix, H. Li, T. M. Koh, W. L. Leong, S. Powar, A. C. Grimsdale, M. Grätzel, N. Mathews and S. G. Mhaisalkar, *J. Mater. Chem. A*, 2014, **2**, 6305.
28 N. J. Jeon, J. Lee, J. H. Noh, M. H. Nazeeruddin, M. Grätzel and S. I. Seok, *J. Am. Chem. Soc.*, 2013, **135**, 19087.
29 J. H. Heo, S. H. Im, J. H. Noh, T. N. Mandal, C. S. Lim, J. Chang, Y. H. Lee, H. J. Kim, A. Sarkar, M. K. Nazeeruddin, M. Grätzel and S. Seok, *Nat. Photonics*, 2013, **7**, 486.
30 H. Chou, H. Shih and C. Cheng, *J. Mater. Chem.*, 2010, **20**, 798.
31 C. Zhang and C.-F. Chen, *J. Org. Chem.*, 2006, **71**, 6626.
32 H. Li, T. M. Koh, A. Hagfeldt, M. Gratzel, S. G. Mhaisalkar and A. C. Grimsdale, *Chem. Commun.*, 2013, **49**, 2409.
33 S. Fantacci, F. D. Angelis, M. K. Nazeeruddin and M. Gratzel, *J. Phys. Chem. C*, 2011, **115**, 23126.
34 R. L. Martin, *J. Chem. Phys.*, 2003, **118**, 4775.
35 R. Tautz, E. Da Como, C. Wiebeler, G. Soavi, I. Dumsch, N. Frohlich, G. Grancini, S. Allard, U. Scherf, G. Cerullo, S. Schumacher and J. Feldmann, *J. Am. Chem. Soc.*, 2013, **135**, 4282.
36 C. M. Cardona, W. Li, A. E. Kaifer, D. Stockdale and G. C. Bazan, *Adv. Mater.*, 2011, **23**, 2367.
37 A. Dualeh, T. Moehl, N. Tétreault, J. Teuscher, P. Gao, M. K. Nazeeruddin and M. Grätzel, *ACS Nano*, 2014, **8**, 362.
38 V. Gonzalez-Pedro, E. J. Juárez-Pérez, W. S. Arsyad, E. M. Barea, F. Fabregat-Santiago, I. Mora-Sero and J. Bisquert, *Nano Lett.*, 2014, **14**, 888.
39 H.-S. Kim, J.-W. Lee, N. Yantara, P. P. Boix, S. A. Kulkarni, S. Mhaisalkar, M. Grätzel and N.-G. Park, *Nano Lett.*, 2013, **13**, 2412–2417.
40 J. Yin, R. F. Chen, S. L. Zhang, H. H. Li, G. W. Zhang, X. M. Feng, Q. D. Ling and W. Huang, *J. Phys. Chem. C*, 2011, **115**, 14778.